Physica Medica 121 (2024) 103357

Contents lists available at ScienceDirect

Physica Medica

journal homepage: www.elsevier.com/locate/ejmp

Development of novel low-cost readout electronics for large field-of-view gamma camera detectors

Aram Radnia [a], Amirhossein Alikhani [a], Behnoosh Teimourian [a], Mahyar Yousef Nejad [a], Mohammad Hossein Farahani [a], Fakhereh Pashaei [b], Arman Rahmim [d,e], Habib Zaidi [f,g,h,i,*,1], Mohammad Reza Ay [a,c,*]

[a] Research Center for Molecular and Cellular Imaging (RCMCI), Advanced Medical Technologies and Equipment Institute (AMTEI), Tehran University of Medical Sciences (TUMS), Tehran, Iran
[b] Institute for Research, Education and Treatment of Cancer, Tehran, Iran
[c] Department of Medical Physics and Biomedical Engineering, Tehran University of Medical Sciences, Tehran, Iran
[d] Departments of Radiology and Physics & Astronomy, University of British Columbia, Vancouver, BC, Canada
[e] Department of Integrative Oncology, BC Cancer Research Institute, Vancouver, BC, Canada
[f] Division of Nuclear Medicine & Molecular Imaging, Geneva University Hospital, CH-1211 Geneva, Switzerland
[g] Department of Nuclear Medicine and Molecular Imaging, University of Groningen, University Medical Center Groningen, Groningen, Netherlands
[h] Department of Nuclear Medicine, University of Southern Denmark, 500 Odense, Denmark
[i] University Research and Innovation Center, Óbuda University, Budapest, Hungary

ARTICLE INFO

Keywords:
Gamma camera
Square PMT
Readout electronics
NEMA NU 1-2018

ABSTRACT

Purpose: Large scintillation crystals-based gamma cameras play a crucial role in nuclear medicine imaging. In this study, a large field-of-view (FOV) gamma detector consisting of 48 square PMTs developed using a new readout electronics, reducing 48 (6 × 8) analog signals to 14 (6 + 8) analog sums of each row and column, with reduced complexity and cost while preserving image quality.
Methods: All 14 analog signals were converted to digital signals using AD9257 high-speed analog to digital (ADC) converters driven by the SPARTAN-6 family of field-programmable gate arrays (FPGA) in order to calculate the signal integrals. The positioning algorithm was based on the digital correlated signal enhancement (CSE) algorithm implemented in the acquisition software. The performance characteristics of the developed gamma camera were measured using the NEMA NU 1-2018 standards.
Results: The measured energy resolution of the developed detector was 8.7 % at 140 keV, with an intrinsic spatial resolution of 3.9 mm. The uniformity was within 0.6 %, while the linearity was within 0.1 %.
Conclusion: The performance evaluation demonstrated that the developed detector has suitable specifications for high-end nuclear medicine imaging.

1. Introduction

Given the extensive use of gamma cameras as a medical diagnostic instrument for characterizing the biodistribution of gamma-emitting radiopharmaceuticals administered to patients [1–3], significant research was carried out to improve the performance of gamma cameras [4]. In a gamma camera, first the gamma rays emitted from the patient's body are collimated using a collimator, subsequently interacting with a monolithic scintillation crystal (commonly used NaI(Tl)). The produced light is converted to a signal by an array of large area photomultiplier tubes (PMTs) located on the opposite side of the crystal. The PMT output pulses are fed into readout electronics to extract the information on both the absorbed energy and the position of the interaction within the crystal [5]. The information is then used to create a 2D distribution map of a radiotracer material administered to the patient. The selected radiotracer is usually a short-lived 99mTc compound [6]. The function of the different organs can be evaluated according to the tracer biodistribution [7,8].

An optimized camera with high uniformity and linearity and good spatial resolution enables improved visual quality and quantitative

* Corresponding authors at: Geneva University Hospital, Division of Nuclear Medicine & Molecular Imaging, Geneva, Switzerland.
E-mail addresses: habib.zaidi@hcuge.ch (H. Zaidi), mohammadreza_ay@tums.ac.ir (M.R. Ay).
[1] ORCID: https://orcid.org/0000-0001-7559-5297.

https://doi.org/10.1016/j.ejmp.2024.103357
Received 27 October 2023; Received in revised form 19 February 2024; Accepted 15 April 2024
Available online 19 April 2024

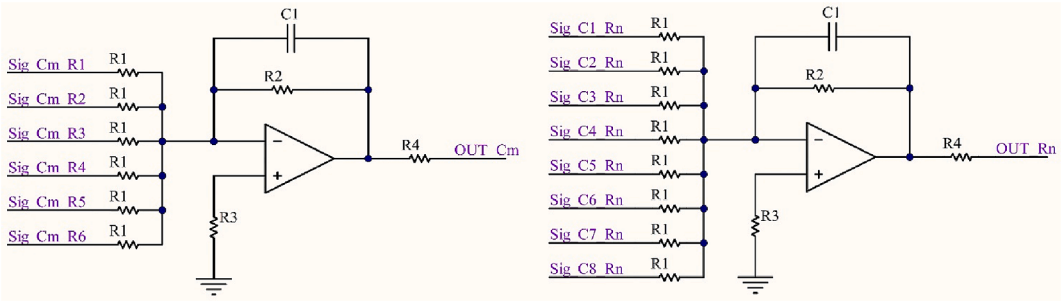

Fig. 1. Column (left) and row (right) summation circuits. Each PMT signal (located on C_mR_n) contributes to two summation circuits ($column_m$ and row_n).

accuracy from the obtained images [9]. The quality of the images is determined by different parameters, such as the scintillation crystal, PMT, light guide, readout electronics, positioning algorithm, calibration algorithms, etc… [10–18]. Multiple positioning algorithms have been developed since 1958 to estimate the 2-D coordinates of the interaction point position in the scintillation crystal [1]. Anger logic, based on the center of gravity algorithm, is a well-known method but suffers from poor spatial resolution and strong FOV compression [14]. Different algorithms have been introduced to improve the spatial resolution in gamma cameras [19–22]. Since square PMTs were used in developed detector, the correlated signal enhancement (CSE) method was chosen as the positioning method. The digital CSE positioning algorithm achieves the best performance with square PMT-based gamma cameras [19,21]. In this algorithm, the rows and the columns of the PMT signals are summed, and subsequently, CSE processes two one-dimensional (1D) outputs to achieve a two-dimensional (2D) position (x and y) for each event.

Today, gamma camera read-out circuits benefit from full digital methods of processing and analyzing the PMT signal due to gaining higher energy and spatial resolution. In large area detectors equipped with a high number of PMTs, full digital methods increase the complexity of read-out circuits, for example, requiring a high number of fast ADCs as well as fast current amplifiers, more professional processor, more complex circuit design, and so forth, resulting in a more expensive acquisition board. By introducing a combination of digital and analog read-out electronics for systems with PMTs, the complexity and the cost can be decreased. The majority of gamma cameras commonly use an array of $N \times M$ PMTs, each one producing a separate signal. To date, many techniques have been developed to multiplex these individual signals [23]. In this study, a new readout electronics is introduced which reduce $N \times M$ analog signals into an $N + M$ analog sum of each row and column. This method reduces analog and digital complexities enabling improved cost design. In what follows, used methods are elaborated and the performance of the developed gamma camera is evaluated.

2. Materials and methods

2.1. Gamma camera

Developed gamma camera utilizes large square PMTs (R6237, Hamamatsu, Japan) and includes an NaI (Tl) crystal with an area of 58 $\times$ 42 cm^2 with a thickness of 9.5 mm attached to an 18-mm thick glass

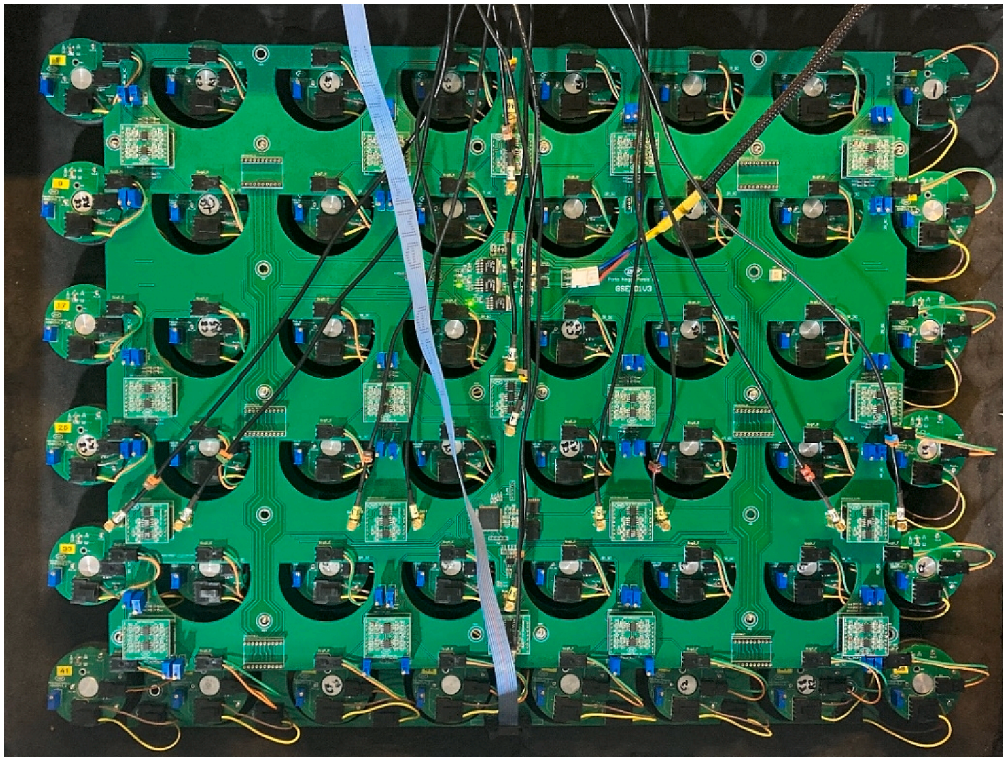

Fig. 2. Developed pizza board consisting of preamps and summation circuits. Each preamp is placed close to the corresponding PMT to minimize track length and noise.

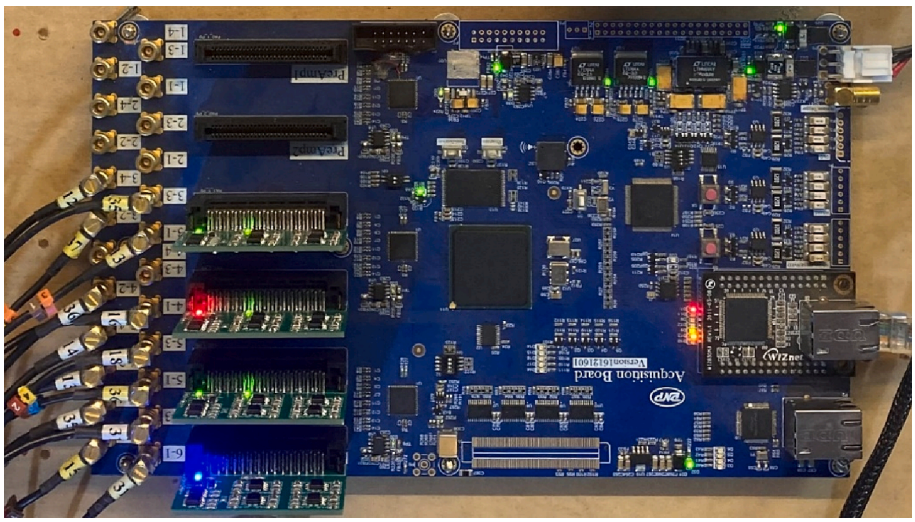

Fig. 3. Developed ACQ board consisting of high-speed ADCs, FPGA and WIZnet.

light guide followed by an arrangement of 6 × 8 square PMTs measuring 76 × 76 mm^2 in area. A Silicon-based compound is used as an optical adhesive to improve the optical coupling between the crystal and the PMTs.

2.2. Readout electronics

The large area gamma camera on which this readout method is implemented has 48 large square PMT arranged in a 6 × 8 matrix array. First, the generated signals of the PMTs were amplified with a series of 48 fast current-feedback amplifiers, and the current signals of PMTs were converted to voltage signals. The amplifier circuit is an amplifier that uses a capacitor in feedback, "a charge sensitive amplifier." The length of the PMT voltage signals can be adjusted by changing the value of the feedback capacitor in the amplifier circuit. The length of the signal is set to 1 μsec to achieve the best quality of signal while preventing signal overlap.

Subsequently, a circuit has been designed to sum up the PMT's signals by rows and columns in an analog way. This circuit is a resistor network containing the same value of resistances. A schematic of this circuit is shown for the row and column in Fig. 1. By utilizing analog summation, six signals presenting the sum of row PMTs and eight signals presenting the sum of column PMTs, or 14 signals in total, will be generated instead of 48 signals representing each of the PMTs in the traditional full digital methods.

All amplification and summation circuits are in the pizza board and its daughter boards inside the detector (Fig. 2).

Next, these 14 voltage signals are transformed into differential signals to enhance the SNR in conveying these signals to the analog-to-digital converter (ADC) to be sampled into digital signals. The ADC utilized in the acquisition board is AD9257 (Analog Devices, U.S.A.), which has an 8-channel input, up to 65 MHz sample rate, 14 bits sampling resolution, and serial output format. The sampling rate of ADCs is set at 20 million samples per second to ensure the quality of sampling and meet the Nyquist frequency. Since the output channels of the ADCs operate in serial mode and transmit data at the rising edge as well as the falling edge of the clock, the frequency of transmitting data from ADC output channels is 140 MHz. As such, it is crucial that the length of all paths from ADC output channels (every 14 of them) to the field-programmable gate array (FPGA) chip be the same to ensure the concurrency of the digital signals. The FPGA utilized in the signal acquisition board is XC6SLX100 of the SPARTAN-6 family (Xilinx, U.S.A.). All ADCs and FPGA are in the ACQ board (Fig. 3). In traditional full digital methods, the cost of converting 48 channels to digital signals is higher because it would require more ADCs and more complicated FPGA code.

The DC value of the digital row/column signals is not constant; rather, it continuously changes at a slow pace. Additionally, some fluctuations and disturbances can be seen in these signals. Subsequently, a pulse DC-rejection module was designed on the FPGA to be immune to sudden and significant changes in the signal value and follow the DC value changes correctly over time. After the DC-rejection module, to measure the value of the row/column AC signals, the threshold pulse integration technique was used to calculate the pulse area of these signals. The obtained integrations were then transmitted to the acquisition computer software for positioning through the UDP Ethernet protocol via the W5300 (WIZnet) chip, and the module that provided this transmission was implemented on the FPGA. The software to perform linearity, energy, and uniformity calibrations and to quantitatively evaluate planar images was written in Python.

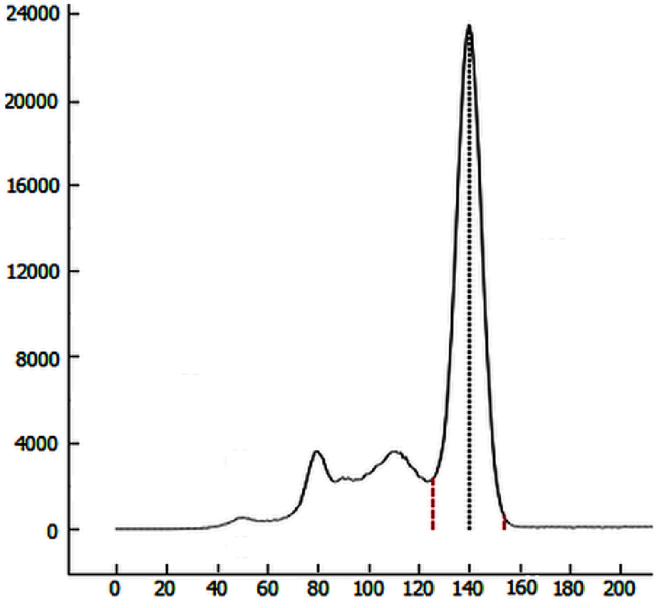

Fig. 4. Energy spectrum after energy calibration showing clearly visible Tc-99 m 140 keV photopeak.

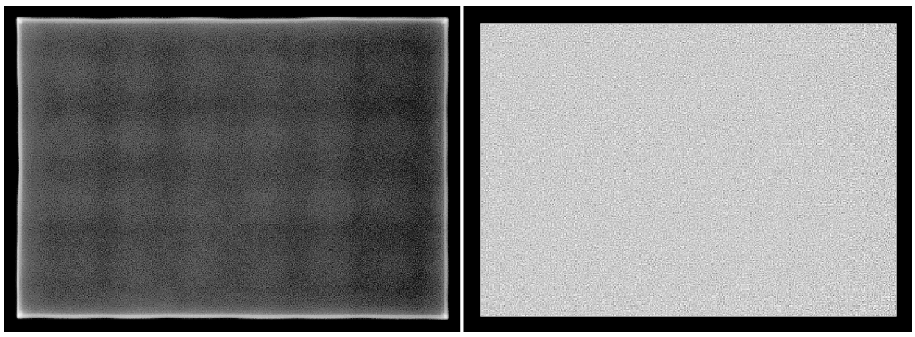

Fig. 5. Flood image before (left) and after (right) uniformity calibration. As expected, at the edge area of the detector, the intensity is high due to lack of positioning data. This area is masked after calibration.

Table 1
Summary of the results achieved for the intrinsic flood field uniformity of the detectors.

Intrinsic flood field uniformity	Value
Differential CFOV (%)	0.4
Differential UFOV (%)	0.4
Integral CFOV (%)	0.4
Integral UFOV (%)	0.6

2.3. Positioning

The positioning algorithm utilized to determine the position of the hit gamma-ray into the gamma camera's surface was based on the digital CSE algorithm, because in gamma cameras equipped with large square PMTs, other positioning algorithms, such as Anger's algorithm require more sophisticated correction techniques. The digital CSE algorithm requires column and row summation of PMT signals; this algorithm performs two identical processes to determine the position of each event in one-dimension (1D), and then combines the results of these two processes to produce a two-dimensional (2D) (x and y) position of this event. This algorithm is implemented on the acquisition software on a computer. It processes the x position of each event by getting eight summed-up column signals and obtains the y position of the events by getting six summed-up row signals. All input values are summed up and stored as energy values.

2.4. Calibration

The first step is to adjust the PMTs gain. Then, 2D linearity calibration data acquired with a well-collimated beam of gamma rays normal to the face is needed. Two lead masks with parallel vertical and horizontal slits 1 mm in width and spaced 10 mm from the adjacent ones were used for X and Y linearity calibrations.

The next step was uniformity and energy calibration, and for this purpose a Tc-99 m point source placed far from the detector face. A minimum of 10 k counts for each central pixel must be collected. These calibration methods have been described in previous works [19].

Table 2
Intrinsic values of spatial linearity.

Intrinsic spatial linearity		Value
(Horizontal)	Differential CFOV (mm)	0.04
	Differential UFOV (mm)	0.04
	Absolute CFOV (mm)	0.04
	Absolute UFOV (mm)	0.04
(Vertical)	Differential CFOV (mm)	0.03
	Differential UFOV (mm)	0.04
	Absolute CFOV (mm)	0.1
	Absolute UFOV (mm)	0.1

3. Results

The performance characteristics of the developed detector were characterized using the NEMA NU 1-2018 standard [24]. For this purpose, energy resolution, spatial linearity, spatial resolution, and uniformity were measured. In the developed detector, the useful field-of-view (UFOV) is 54 × 38 cm^2, whereas the central field-of-view (CFOV) is 46.7 × 32.9 cm^2.

The energy spectrum was measured based on NEMA standards. The full width at half-maximum (FWHM) energy was 13 % before calibration and 8.7 % after calibration. Fig. 4 shows the energy spectrum for Tc-99 m at 140 keV after energy calibration. The sensitivity was 78cps/MBq on Low Energy High Resolution (LEHR) collimator surface.

The uniformity of the detector was measured by placing a point source far from its face. Fig. 5 shows the flood-field image before and after uniformity calibration. The intrinsic flood-field uniformity was measured according to the NEMA NU 1-2018 standard protocol [24]. The results are summarized in Table 1.

Fig. 6 shows the slit mask lead images after calibrations. The intrinsic

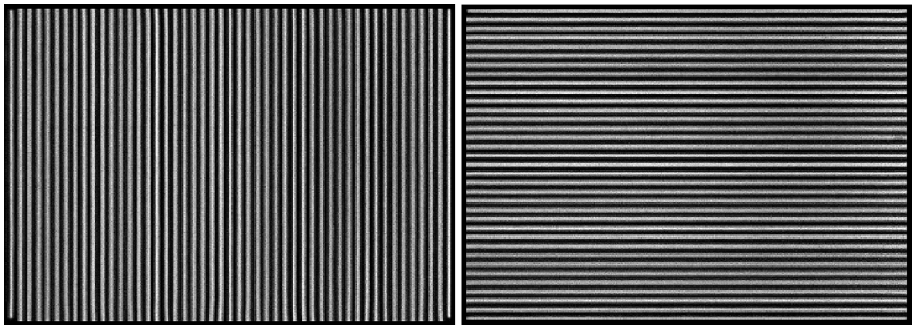

Fig. 6. Vertical (left) and horizontal (right) slit mask lead images after calibrations.

Table 3
Intrinsic values of spatial resolution in the useful and central fields-of-view.

INTRINSIC SPATIAL RESOLUTION		Value
(Horizontal)	FWHM CFOV (mm)	3.9
	FWHM UFOV (mm)	3.9
	FWTM CFOV (mm)	6.9
	FWTM UFOV (mm)	7.0
(Vertical)	FWHM CFOV (mm)	3.7
	FWHM UFOV (mm)	3.7
	FWTM CFOV (mm)	6.8
	FWTM UFOV (mm)	6.8

Table 4
Comparison of the developed detector with other similar detectors.

Specification	**Developed Detector**	**Discovery NM630 GE** [25]	**Infinia GE** [26]	**Symbia S Siemens** [27]
Crystal	NaI(Tl)	NaI(Tl)	NaI(Tl)	NaI(Tl)
Thickness (mm)	9.5	9.5	9.5	9.5
PMT shape	Square	Circular	Circular	Hexagonal
PMT size (mm)/pcs	76/48	76/53 38/6	76/53 38/6	76/53 51/6
UFOV (cm^2)	54 × 38	54 × 40	54 × 40	53.3 × 38.7
Intrinsic Spatial Resolution in CFOV (mm)	≤ 3.9	≤ 3.8	≤ 3.8	≤ 3.8
Intrinsic Energy Resolution (%)	≤ 8.7	≤ 9.5	≤ 9.8	≤ 9.9
Differential Linearity in UFOV (mm)	≤ 0.04	≤ 0.2	≤ 0.1	≤ 0.2
Absolute Linearity in UFOV (mm)	≤ 0.1	≤ 0.5	≤ 0.5	≤ 0.7
Differential Uniformity in UFOV (%)	≤ 0.4	≤ 2.3	≤ 2.3	≤ 2.7
Integral Uniformity in UFOV (%)	≤ 0.6	≤ 3.6	≤ 3.6	≤ 3.7

differential linearity was measured as the standard deviation (SD) of peak locations in slit images. The intrinsic absolute linearity was measured as the maximum displacement of peaks in comparison with parallel lines spaced 10 mm apart fitted to the image. The results regarding intrinsic spatial linearity are available in Table 2. To measure the intrinsic spatial resolution (without collimator), an image of 1-mm wide slits spaced 10 mm from the adjacent ones was used. The FWHM and full width at tenth maximum (FWTM) was calculated using the extracted line spread function (LSF) of each line as spatial resolution. The intrinsic spatial resolution results are reported in Table 3.

4. Discussion

In this study, a gamma camera detector using large square PMTs which minimizes the required number of PMTs to cover the crystal area is introduced. 6 × 8 analog signals were also reduced into 6 + 8 analog sum of each row and column, enabling reduced analog and digital complexities and improved cost. 14 signals 1 μsec in length converted to digital using AD9257 high-speed ADCs. The SPARTAN-6 family of FPGA was used to drive ADCs at a rate of 20 million samples per second and to calculate integral values of 14 channels after DC-rejection. Subsequently, the obtained integrations were transmitted to the acquisition computer software for positioning through the UDP Ethernet protocol. The positioning algorithm was based on the digital CSE algorithm which was implemented in the acquisition software.

The performance characteristics of the developed gamma camera were measured using the NEMA NU 1-2018 standard. The measured energy resolution in the developed detector was 8.7 %, intrinsic spatial resolution was 3.9 mm, uniformity was within 0.6 %, and linearity was within 0.1 %. The developed detector's parameters compared with the GE Discovery NM630 [25], GE Infinia [26], and Siemens Symbia S [27]. The properties of all detectors are summarized in Table 4. All detectors had similar NaI(Tl) crystal thickness and UFOV area (within 5 %). The detector had 48 square PMTs, while others had a total of 59 PMTs (circular and hexagonal). Using square PMT, the detector showed superior energy resolution, because it left no uncovered area. Spatial resolution was in good agreement with the other detectors, in comparison with non-square PMTs. The linearity and the uniformity were superior to the reported designs. The performance evaluation showed that the developed detector has proper specifications for imaging purposes at a lower cost and with less complexity.

5. Conclusion

In this study, we introduced a new readout electronics for scintillation detectors using square PMTs. Our approach combined analog and digital signals in positioning, reduced 48 signals to 14 signals and improved complexity and cost considerations, while preserving image quality. The NEMA NU 1-2018 results confirmed that the designed gamma detector had excellent performance and can be used reliably for nuclear medicine imaging applications. Future challenges would be to add another analog circuit to PMTs signal before summation and digitization for automatic PMTs amplitudes tunning.

Declaration of competing interest

The authors declare that they have no known competing financial interests or personal relationships that could have appeared to influence the work reported in this paper.

Acknowledgments

This work was supported by Tehran University of Medical Sciences, Grant No. 1401-3-424-63878.

References

[1] Anger HO. Scintillation camera. Rev Sci Instrum 1958;29:27–33.
[2] Cherry SR, Sorenson JA, Phelps ME, ScienceDirect (Online service). Physics in Nuclear Medicine. Saunders; 2003.
[3] Chandra R, Rahmim A. Nuclear medicine physics: the basics. Lippincott Williams & Wilkins; 2017.
[4] Peterson TE, Furenlid LR. SPECT detectors: the Anger Camera and beyond. Phys Med Biol 2011;56:R145.
[5] Anger HO. Scintillation camera with multichannel collimators. J Nucl Med 1964;5:515–31.
[6] Boschi A, Uccelli L, Martini P. A picture of modern Tc-99m radiopharmaceuticals: production, chemistry, and applications in molecular imaging. Appl Sci 2019;9:2526.
[7] Rassam F, Olthof PB, Bennik RJ, van Guilk TM. Current modalities for the assessment of future remnant liver function. Visc Med 2017;33:442–8.
[8] Park J, Bae S, Seo S, Park S, Bang J-I, Han JH, et al. Measurement of glomerular filtration rate using quantitative SPECT/CT and deep-learning-based kidney segmentation. Sci Rep 2019;9:4223.
[9] Hutton BF, Erlandsson K, Thielemans K. Advances in clinical molecular imaging instrumentation. Clin Transl Imaging 2018;6:31–45.
[10] Cherepy NJ, Payne SA, Asztalos SJ, Hull G, Kuntz JD, Niedermayr T, et al. Scintillators with potential to supersede lanthanum bromide. IEEE Trans Nucl Sci 2009;56:873–80.
[11] Dorenbos P, de Haas JTM, Van Eijk C. Non-proportionality in the scintillation response and the energy resolution obtainable with scintillation crystals. IEEE Trans Nucl Sci 1995;42:2190–202.
[12] Hemmati H, Kamali-Asl A, Haghshenas R. The effects of light guide thickness on the accuracy of position estimation, linearity, and uniformity responses of anger camera: A Monte Carlo study. Front Biomed Technol 2015;2:172–83.
[13] Wang B, Kreuger R, Beekman FJ, Goorden MC. Novel light-guide-PMT geometries to reduce dead edges of a scintillation camera. Phys Med 2018;48:84–90.
[14] Pani R, Bettiol M, Preziosi E, Cinti M, Borrazzo C, Pellegrini R, et al. Position algorithm for monolithic scintillation crystals based on charge projection readout. J Instrum 2016;11:C01061.

[15] Galasso M, Fabbri A, Borrazzo C, Cencelli VO, Pani R. A theoretical model for fast evaluation of position linearity and spatial resolution in gamma cameras based on monolithic scintillators. IEEE Trans Nucl Sci 2016;63:1386–98.
[16] Barrett HH, Hunter WC, Miller BW, Moore SK, Chen Y, Furenlid LR. Maximum-likelihood methods for processing signals from gamma-ray detectors. IEEE Trans Nucl Sci 2009;56:725–35.
[17] España S, Deprez K, Van Holen R, Vandenberghe S. Fast calibration of SPECT monolithic scintillation detectors using un-collimated sources. Phys Med Biol 2013; 58:4807.
[18] Hung NM, Joung J, Lee K, Kim Y. Development of correction schemes for a small field of view gamma camera. Biomed Eng Lett 2012;2:215–22.
[19] Zeraatkar N, Sajedi S, Fard BT, Kaviani S, Akbarzadeh A, Farahani M, et al. Development and calibration of a new gamma camera detector using large square Photomultiplier Tubes. J Instrum 2017;12:P09008.
[20] Ling T, Lewellen T, Miyaoka R. Depth of interaction decoding of a continuous crystal detector module. Phys Med Biol 2007;52:2213.
[21] Teimourian Fard B, Shamsaei Zafarghandi M. Comparative assessment of the accuracy of maximum likelihood and correlated signal enhancement algorithm positioning methods in gamma camera with large square photomultiplier tubes. Iran J Nucl Med 2019;27:81–6.
[22] Aliaga R, Martinez J, Gadea R, Sebastia A, Benlloch J, Sánchez F, et al. Corrected position estimation in PET detector modules with multi-anode PMTs using neural networks. IEEE Trans Nucl Sci 2006;53:776–83.
[23] Pierce L, Hunter W, Haynor D, MacDonald L, Kinahan P, Miyaoka R. Multiplexing strategies for monolithic crystal PET detector modules. Phys Med Biol 2014;59: 5347.
[24] National Electrical Manufacturers Association. NEMA Standards Publication NU 1-2018: Performance Measurements of Gamma Cameras. Rosslyn Virginia: National Electrical Manufacturers Association; 2018.
[25] GE Healthcare Discovery NM630 Datasheet, 5410645-IEN Rev.1, DOC0963080_ Rev 3.0.
[26] GE Healthcare Infinia Product data, Release 2.5, Direction 2411980-100 Rev3, 2006.
[27] Siemens Svmbia S system specification, Order No. A91M1-10128-4T-7600, 2010.